J. Fluid Mech. (2001), *vol.* 447, *pp.* 111–128. © 2001 Cambridge University Press
DOI: 10.1017/S002211200100581X Printed in the United Kingdom

Fluid instabilities in precessing spheroidal cavities

By S. LORENZANI AND A. TILGNER

Institute of Geophysics, University of Göttingen, Herzberger Landstrasse 180,
D-37075 Göttingen, Germany

(Received 23 October 2000 and in revised form 5 March 2001)

We study by direct numerical simulation the motion of incompressible fluid contained in an ellipsoid of revolution with ellipticity 0.1 or less which rotates about its axis of symmetry and whose rotation axis is executing precessional motion. A solution to this problem for an inviscid fluid given by Poincaré (1910) predicts motion of uniform vorticity. The simulations show how the orientation of the average vorticity of a real fluid is influenced by both pressure and viscous torques exerted by the boundaries. Axisymmetric shear layers appear which agree well with those observed experimentally by Malkus (1968). Shear caused by deviations from a velocity field with uniform vorticity triggers an instability consisting of waves propagating around the average rotation axis of the fluid. The Ekman layers at the boundaries may also become unstable.

1. Introduction

Motion of incompressible fluid in a rotating and precessing spheroidal cavity is a central problem for several areas of astrophysics, geophysics and engineering. Without the precessing motion of the container, the fluid would simply be entrained by viscous forces until it rotated uniformly like a solid body. Precession disturbs the solid body rotation. In the geophysical application, the resulting flow is used as a model for the response of the liquid core to the Earth's precession. Interest in this driving mechanism has been maintained over recent years by the proposal that precession might power the geodynamo. Since the basic solution to the fluid dynamic problem is nearly toroidal, dynamo action can only be expected in unstable flows. Instabilities have been observed in experiments with water-filled precessing ellipsoidal containers. The numerical simulations presented here are intended to complement the limited experimental observations which are available regarding the structure of the instability.

Most modern literature refers to Poincaré's (1910) work as the starting point for today's investigation of precession-driven motion. Poincaré assumed an ideal fluid inside the Earth and showed that flows with constant vorticity are solutions of the equation of motion for zero viscosity. However, viscosity modifies Poincaré's solution in that boundary layers appear, and more surprisingly, zones of strong shear also appear in the bulk of the flow which do not vanish in the limit of viscosity tending to zero (Busse 1968). Experiments (Malkus 1968; Vanyo *et al.* 1995) have shown that at high enough precession rates, the internal shear layers develop a wavelike instability, and in a second transition, the entire flow becomes turbulent.

The available computer capacities preclude a systematic survey of the parameter space. The original experiments by Malkus (1968) are closest to the computationally accessible range of parameters. The calculations presented below are chosen in order to reproduce these experiments reasonably well.

In a first experiment with an axisymmetric container of ellipticity e equal to 0.04 (precise definitions of the control parameters will be given in the next section), the angle between container and precession axes was 30°. As the (retrograde) precession Ω_p was increased at a constant Ekman number of 2.5×10^{-6} (based on the 'diurnal' rotation rate ω_D of the ellipsoid about its symmetry axis), laminar flow was observed at $\Omega_p/\omega_D = -0.0125$, wavy distortions of the internal shear layers at $\Omega_p/\omega_D = -0.0167$ and increasingly disorganized flow at higher precession rates. A second experiment used an ellipsoid of ellipticity 0.1 with an angle between precession and container axes of 96° at an Ekman number of 2×10^{-6}. The onset of a wavelike instability was again observed (at $\Omega_p/\omega_D = 0.01 - 0.013$), this time followed by a sudden transition to more violent motion around $\Omega_p/\omega_D = 0.05$ during which the torque necessary to maintain the container's motion abruptly increased. This second transition showed hysteresis.

Another series of experiments was motivated by an engineering application (Vanyo *et al.* 1995 and references therein). A wavy instability of internal shear layers is also reported by Vanyo *et al.* (1995) at lower Ekman numbers, precession rates and ellipticities than in Malkus' experiments. Vanyo *et al.* (1995) and Vanyo & Dunn (2000) used containers with ellipticities 1/400 and 1/100 and an angle between container axis and precession vector of 23.5°. They sampled the parameter range of Ekman numbers larger than or equal to 7×10^{-7} and non-dimensional precession rates between 10^{-6} and 10^{-2}.

Malkus (1968) suggested that the initial instability and its further development into turbulence originate from cylindrical shear layers. Kerswell (1993) later pointed out that the Poincaré solution is also prone to inertial instabilities. This second mechanism is not effective in spheres.

After a description of the numerical method in the next section, § 3 will explore the basic flow and the structure of the internal shear layers. The instabilities and in particular the onset of wave disturbances are dealt with in § 4.

2. Numerical methods

The numerical challenge consists in computing the stability boundary of a rapidly rotating fluid in an ellipsoidal shell. The problem profits from a high-order method so that a high accuracy is obtained per grid point and in order to keep numerical diffusivity to a minimum. The obvious choice is a spectral method. These methods however face the problem of a boundary geometry which is not easily accommodated by any standard coordinate system. Previous attempts at embedding the ellipsoidal fluid volume in a spherical computational volume have not been successful beyond linearized equations of motion (Tilgner 1999*b*). A different approach is used here: the ellipsoidal fluid volume is distorted by a coordinate transformation into a spherical domain; the transformed equations are then discretized with the help of spherical harmonics for the angular variables and with Chebychev polynomials in the radial direction. Only aspects of the method peculiar to elliptic boundaries are emphasized in this section since detailed descriptions of the code for spherical geometry have been given elsewhere (Tilgner 1999*c*).

In the following, two coordinate systems will be used: the original one in which the boundaries are ellipsoids of revolution and the computational one in which the boundaries are spherical. The first system will be described by symbols with tildes. Consider incompressible fluid of kinematic viscosity ν in an ellipsoidal shell rotating with angular frequency ω_D about the z-axis. The shell furthermore executes precessional motion characterized by the precession vector $\Omega_p \hat{\boldsymbol{\Omega}}_p$ (hats denote unit vectors). The boundaries of the shell are given by

$$\frac{\tilde{x}^2}{a^2} + \frac{\tilde{y}^2}{a^2} + \frac{\tilde{z}^2}{c^2} = 1, \tag{1a}$$

$$\frac{\tilde{x}^2}{(\eta a)^2} + \frac{\tilde{y}^2}{(\eta a)^2} + \frac{\tilde{z}^2}{(\eta c)^2} = 1; \tag{1b}$$

$\eta < 1$ and both boundaries have the same ellipticity $e = 1 - c/a$. Units of length and time are chosen as $(1-\eta)a$ and $1/\omega_D$, respectively. Again using tildes to denote the dimensionless quantities, the equation of motion for the velocity $\tilde{\boldsymbol{u}}(\tilde{\boldsymbol{r}}, t)$ reads in a frame of reference attached to the shell

$$\frac{\partial}{\partial t} \tilde{\nabla} \times \tilde{\boldsymbol{u}} + \tilde{\nabla} \times \{(2(\hat{\tilde{z}} + \boldsymbol{\Omega}) + \tilde{\nabla} \times \tilde{\boldsymbol{u}}) \times \tilde{\boldsymbol{u}}\} = E \tilde{\nabla}^2 \tilde{\nabla} \times \tilde{\boldsymbol{u}} + 2\hat{\tilde{z}} \times \boldsymbol{\Omega}, \tag{2}$$

$$\tilde{\nabla} \cdot \tilde{\boldsymbol{u}} = 0. \tag{3}$$

The Ekman number E is defined by $E = \nu(\omega_D (1-\eta)^2 a^2)^{-1}$ and $\boldsymbol{\Omega} = \Omega_p/\omega_D \hat{\boldsymbol{\Omega}}_p$. The computational coordinate system is now introduced by the transformations

$$x = \tilde{x}, \quad y = \tilde{y}, \quad z = \frac{\tilde{z}}{1-e}, \tag{4}$$

If the velocities are transformed likewise,

$$u_x = \tilde{u}_x, \quad u_y = \tilde{u}_y, \quad u_z = \frac{\tilde{u}_z}{1-e}, \tag{5}$$

one obtains again a solenoidal vector field, $\nabla \cdot \boldsymbol{u} = 0$. The boundaries are now given by

$$x^2 + y^2 + z^2 = r_o^2, \tag{6a}$$

$$x^2 + y^2 + z^2 = r_i^2, \tag{6b}$$

with $r_i/r_o = \eta$ and $r_o - r_i = 1$. In this new formulation, the problem lends itself to a spectral discretization in spherical harmonics. However, the equation of motion in the computational coordinate system is more complicated:

$$\frac{\partial}{\partial t} \nabla \times \boldsymbol{u} - E \nabla^2 \nabla \times \boldsymbol{u} + \boldsymbol{L} = -\nabla \times \boldsymbol{N} + e \nabla \times (N_z \hat{z}) + 2(1-e)\hat{z} \times \boldsymbol{\Omega}. \tag{7}$$

The nonlinear and Coriolis terms have been grouped together, as have the linear terms which vanish for $e = 0$:

$$\boldsymbol{N} = (2(\hat{\tilde{z}} + \boldsymbol{\Omega}) + \tilde{\nabla} \times \tilde{\boldsymbol{u}}) \times \tilde{\boldsymbol{u}}, \tag{8}$$

$$\begin{aligned} \boldsymbol{L} = e(e-2) \frac{\partial}{\partial t} \nabla \times (u_z \hat{z}) - E \frac{e(2-e)}{(1-e)^2} \frac{\partial^2}{\partial z^2} \nabla \times \boldsymbol{u} \\ - E \left[e(e-2)\nabla^2 - \left(\frac{e(e-2)}{1-e} \right)^2 \frac{\partial^2}{\partial z^2} \right] \nabla \times (u_z \hat{z}). \end{aligned} \tag{9}$$

The precession axis $\hat{\boldsymbol{\Omega}}$ forms the angle α $(0 < \alpha < \pi/2)$ with the z-axis and is time dependent in the chosen system of reference:

$$\hat{\boldsymbol{\Omega}} = \sin\alpha\cos t\,\hat{\boldsymbol{x}} - \sin\alpha\sin t\,\hat{\boldsymbol{y}} + \cos\alpha\,\hat{\boldsymbol{z}}. \tag{10}$$

The boundary conditions require that $\boldsymbol{u} = 0$ at $r = r_i, r_o$. The solenoidal vector field $\boldsymbol{u}$ can be written in terms of poloidal and toroidal scalars Φ and Ψ:

$$\boldsymbol{u} = \nabla \times \nabla \times (\Phi\hat{\boldsymbol{r}}) + \nabla \times (\Psi\hat{\boldsymbol{r}}) \tag{11}$$

which are then decomposed into spherical harmonics:

$$\left.\begin{aligned} \Phi &= r\sum_{l=1}^{\infty}\sum_{m=-l}^{l} V_l^m(r,t)P_l^m(\cos\theta)\mathrm{e}^{\mathrm{i}m\varphi}, \\ \Psi &= r^2\sum_{l=1}^{\infty}\sum_{m=-l}^{l} W_l^m(r,t)P_l^m(\cos\theta)\mathrm{e}^{\mathrm{i}m\varphi}. \end{aligned}\right\} \tag{12}$$

Operating with $\hat{\boldsymbol{r}}\cdot$ and $\hat{\boldsymbol{r}}\cdot\nabla\times$ on (7) one obtains two equations for $V_l^m(r,t)$ and $W_l^m(r,t)$:

$$\begin{aligned} &\frac{\partial}{\partial t}\mathscr{D}_l V_l^m - E\,\mathscr{D}_l^2 V_l^m - \frac{r}{l(l+1)}[\hat{\boldsymbol{r}}\cdot\nabla\times\boldsymbol{L}]_l^m \\ &\qquad = \frac{r}{l(l+1)}[\hat{\boldsymbol{r}}\cdot\nabla\times\{\nabla\times\boldsymbol{N} - e\nabla\times(N_z\hat{\boldsymbol{z}})\}]_l^m, \end{aligned} \tag{13a}$$

$$\begin{aligned} &\frac{\partial}{\partial t}W_l^m - E\left(\frac{\partial^2}{\partial r^2} + \frac{4}{r}\frac{\partial}{\partial r} + \frac{2-l(l+1)}{r^2}\right)W_l^m + \frac{1}{l(l+1)}[\hat{\boldsymbol{r}}\cdot\boldsymbol{L}]_l^m \\ &\qquad = -\frac{1}{l(l+1)}[\hat{\boldsymbol{r}}\cdot\{\nabla\times\boldsymbol{N} - e\nabla\times(N_z\hat{\boldsymbol{z}})\}]_l^m + (1-e)[f]_l^m, \end{aligned} \tag{13b}$$

with

$$\mathscr{D}_l = \frac{\partial^2}{\partial r^2} + \frac{2}{r}\frac{\partial}{\partial r} - \frac{l(l+1)}{r^2}, \qquad f = \tfrac{1}{2}\Omega\sin\alpha[\mathrm{i}P_1^1\mathrm{e}^{\mathrm{i}(\varphi+t)} + \text{c.c.}].$$

$[\;]_l^m$ denotes the l,m-component of the quantity in the square bracket. These equations need to be solved subject to the boundary conditions

$$V_l^m = \frac{\partial V_l^m}{\partial r} = W_l^m = 0 \qquad \text{at} \qquad r = r_i, r_o. \tag{14}$$

In order to complete the discretization, the sums in (12) are truncated at L to include only terms with $l \leqslant L$ and the functions V_l^m and W_l^m are expanded in N_r Chebychev polynomials T_n as

$$V_l^m(r,t) = \sum_{n=0}^{N_r-1} v_{l,n}^m(t)T_n(x), \quad W_l^m(r,t) = \sum_{n=0}^{N_r-1} w_{l,n}^m(t)T_n(x), \tag{15}$$

with $x = 2(r - r_i) - 1$. The collocation points are placed in direct space such that a fast cosine transform can be used to switch between physical and spectral space. Equations (13a,b) are enforced at every collocation point and the spectral representation in radius is merely used to compute derivatives.

Let $y(t)$ be a vector containing the coefficients $v_{l,n}^m(t)$ and $w_{l,n}^m(t)$. If equations (13a) and (13b) are discretized in time using implicit Euler steps and second-order Adams–Bashforth steps for the linear and nonlinear terms, respectively, they can be written for a time step of size h in the form

$$\boldsymbol{My}(t+h) = \boldsymbol{M}'\boldsymbol{y}(t) + \tfrac{1}{2}h[3\boldsymbol{nl}(\boldsymbol{y}(t)) - \boldsymbol{nl}(\boldsymbol{y}(t-h))], \tag{16}$$

where $\boldsymbol{M}$ and $\boldsymbol{M}'$ represent matrices and $\boldsymbol{nl}$ all nonlinear terms and the Coriolis force.

In order to compute the nonlinear terms, $\boldsymbol{u}$, $\nabla \times \boldsymbol{u}$ and $\nabla \times (u_z\hat{\boldsymbol{z}})$ are evaluated in (r, θ, φ)-space. Note that $\boldsymbol{N}$ in (7) is computed in the original coordinates. For this reason, the (r, θ, φ)-components of the three-dimensional vectors are converted into (x, y, z)-components so that e.g. (5) can be easily applied. After all necessary operations have been performed, the result is transformed back into (r, l, m)-space. The radial component of the curl and the radial component of the curl of the curl appearing in (13*a*) and (13*b*) are computed with formulas familiar from simulations in spherical geometry.

For the implicit part of the time step, linear systems of the form

$$\boldsymbol{M}_1\boldsymbol{y} + \boldsymbol{M}_2\boldsymbol{y} = \boldsymbol{A} \tag{17}$$

need to be solved, where $\boldsymbol{M}_1$ represents the discretization of the first two terms in (7), $\boldsymbol{M}_2$ the remaining terms of the left-hand side of (7), and $\boldsymbol{A}$ the right-hand side of (16). $\boldsymbol{M}_1$ decouples in l and m and therefore consists of small blocks which are even independent of m. The corresponding submatrices are computed, inverted and stored for later use during an initialization step. In order to solve the full system, a Jacobi-type iteration is employed:

$$\boldsymbol{y}_{n+1} = \boldsymbol{M}_1^{-1}(-\boldsymbol{M}_2\boldsymbol{y}_n + \boldsymbol{A}) \tag{18}$$

where $\boldsymbol{y}_n$ is the nth iterate of the solution. This aspect of the method leaves room for improvement. The number of iterations necessary to achieve satisfactory accuracy increases with increasing e. In the present application, only small ellipticities are of interest and about 5 iterations are enough to reach convergence so that it did not seem useful to opt for a more powerful method. For $e > 0.2$ however, the Jacobi iteration diverges.

$\boldsymbol{M}_2$ still decouples in m but couples different values of l. It would require a large amount of storage to keep $\boldsymbol{M}_2$ in memory at any one time so that the effect of $\boldsymbol{M}_2$ on $\boldsymbol{y}$ is encoded in a set of subroutines instead. $\boldsymbol{M}_2$ and $\boldsymbol{A}$ contain a multitude of terms in which $\hat{\boldsymbol{r}} \cdot \nabla\times$ and $\hat{\boldsymbol{r}} \cdot \nabla \times \nabla\times$ are applied to expressions in which $u_z\hat{\boldsymbol{z}}$ or second derivatives $\partial^2/\partial z^2$ occur. The three basic subroutines used to compute all these terms take as input the poloidal and toroidal scalars $\tilde{\Phi}$ and $\tilde{\Psi}$ of a vector field $\boldsymbol{v}$ and return the poloidal and toroidal scalars of $\nabla \times \boldsymbol{v}$, $\nabla \times v_z\hat{\boldsymbol{z}}$ or $\nabla \times (\hat{\boldsymbol{z}} \times \boldsymbol{v})$. Note that

$$[\hat{\boldsymbol{r}} \cdot \boldsymbol{v}]_l^m = \frac{l(l+1)}{r^2}[\tilde{\Phi}]_l^m \quad \text{and} \quad [\hat{\boldsymbol{r}} \cdot \nabla \times \boldsymbol{v}]_l^m = \frac{l(l+1)}{r^2}[\tilde{\Psi}]_l^m.$$

For example, $[\hat{\boldsymbol{r}} \cdot \nabla \times u_z\hat{\boldsymbol{z}}]_l^m$ and $[\hat{\boldsymbol{r}} \cdot \nabla \times \nabla \times u_z\hat{\boldsymbol{z}}]_l^m$ are directly given by $l(l+1)/r^2$ times the poloidal and toroidal scalars of $\nabla \times u_z\hat{\boldsymbol{z}}$, respectively. It is easy to see how the terms involving $\partial^2/\partial z^2$ are obtained by noting that

$$\hat{\boldsymbol{r}} \cdot \nabla \times \frac{\partial^2}{\partial z^2}\boldsymbol{u} = \hat{\boldsymbol{r}} \cdot \nabla \times (\hat{\boldsymbol{z}} \times \nabla \times (\hat{\boldsymbol{z}} \times \nabla \times \boldsymbol{u})), \tag{19}$$

and an analogous expression is valid for $\hat{\boldsymbol{r}} \cdot \nabla \times \nabla \times (\partial^2/\partial z^2)\boldsymbol{u}$.

Apart from the special case $e = 0$ nothing seems to be available to comprehensively validate the ellipsoidal code. The program had to be tested term by term by comparing numerical output with calculations made by hand for representative examples of poloidal and toroidal scalars. However, some validation is provided by the agreement between the computed zonal velocity and the experimental observations, and by the comparison with the asymptotic theory of Busse (1968) which will be discussed in the next section.

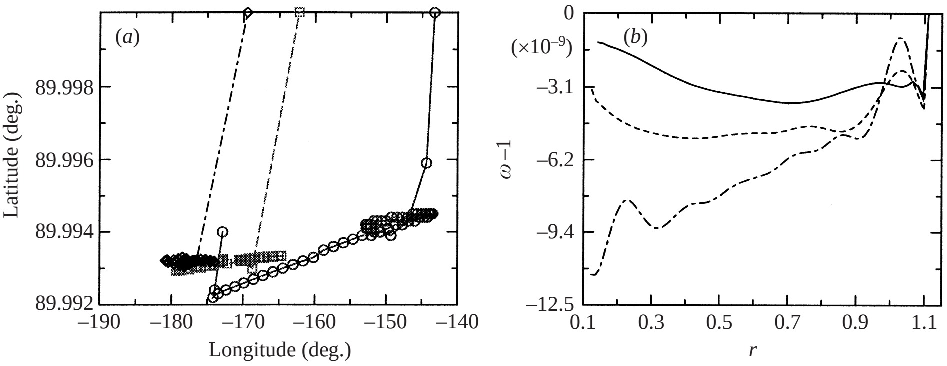

FIGURE 1. (*a*) Latitude and longitude of the direction of the fluid rotation vector $\boldsymbol{\omega}(r)$ (equation (20)) as a function of r for $\Omega = -10^{-5}$, $\alpha = 30°$, $\eta = 0.1$, $e = 0.04$ in the cases $E = 10^{-4}$ (circles), 10^{-5} (squares) and 10^{-6} (diamonds). The symbols mark the direction of $\boldsymbol{\omega}(r)$ at the radii $r_i+((r_o-r_i)/41)n$, $n = 1\ldots41$. The axis of (retrograde) precession points at zero longitude and a latitude of 60°. (*b*) ω, the absolute value of $\boldsymbol{\omega}(r)$ (equation (20)) as a function of r for the same parameters as in (*a*) with the Ekman numbers $E = 10^{-4}$ (solid), 10^{-5} (dashed) and 10^{-6} (dot dashed).

Shells with $\eta = 0.1$ or 0.01 will be used in order to approximate the experimental geometries, as well as an exceptional comparison with an Earth-like shell with $\eta = 0.35$.

3. Basic flows

The structure of the laminar flow in spherical shells has been studied in great detail in Tilgner (1999*a*) and Tilgner & Busse (2001). This section will focus on the influence of the ellipticity of the boundaries and on those features which are relevant for the mechanisms of instability.

In order to quantify the deviations from a solution of uniform vorticity, it is useful to consider a local rotation vector which corresponds to the solid body rotation component of the motion of the fluid at radius r:

$$\boldsymbol{\omega}(r) = \left(1 - e + \frac{1}{1-e}\right)[-\mathrm{Re}\{W_1^1(r)\}\hat{\boldsymbol{x}} + \mathrm{Im}\{W_1^1(r)\}\hat{\boldsymbol{y}}] + W_1^0(r)\hat{\boldsymbol{z}} + \hat{\boldsymbol{z}}. \qquad (20)$$

Re{ } and Im{ } denote the real and imaginary parts of the quantity in curly brackets. The average $\boldsymbol{\omega}_F$ of $\boldsymbol{\omega}(r)$ over the fluid volume can then be compared with the asymptotic theory of Busse (1968). This comparison is made in table 1 for a few representative cases. The agreement is of the same quality as found for spherical shells (Tilgner & Busse 2001). The detail of the variations of $\boldsymbol{\omega}(r)$ for low precession rates is summarized in figure 1. At constant ellipticity, the solution in the bulk of the fluid approaches a state of uniform vorticity as E decreases. At the same time, the orientation of $\boldsymbol{\omega}_F$ progressively rotates into the $(\hat{\boldsymbol{z}}, \hat{\boldsymbol{\Omega}})$-plane. In a sphere however, $\boldsymbol{\omega}_F$ lies nearly perpendicular to the $(\hat{\boldsymbol{z}}, \hat{\boldsymbol{\Omega}})$-plane (see table 1). As E is reduced in an elliptical container, viscous forces become smaller than pressure forces, so that one goes continuously from the orientation characteristic of a sphere to the classical Poincaré solution in which $\boldsymbol{\omega}_F$ lies in the $(\hat{\boldsymbol{z}}, \hat{\boldsymbol{\Omega}})$-plane. These results agree with the purely linear calculations of Tilgner (1999*b*).

Figure 2 shows the velocity field in meridional planes. The most apparent features are non-axisymmetric and include (in panel (*b*)) hints of internal layers emanating

E	e	α (deg.)	Ω	θ_F (deg.)	φ_F (deg.)
10^{-4}	0.04	30	-10^{-5}	5.59×10^{-3} (5.73×10^{-3})	−149.76 (−148.40)
10^{-5}	0.04	30	-10^{-5}	6.70×10^{-3} (6.88×10^{-3})	−169.47 (−168.52)
10^{-6}	0.04	30	-10^{-5}	6.77×10^{-3} (7.11×10^{-3})	−176.76 (−176.27)
10^{-5}	0	30	-10^{-5}	3.65×10^{-2} (3.44×10^{-2})	−104.51 (−95.59)
10^{-4}	0.04	30	-10^{-3}	0.568 (0.581)	−149.25 (−147.87)
10^{-4}	0.04	30	-10^{-2}	6.62 (6.73)	−143.77 (−141.97)
10^{-4}	0.04	30	−0.03	31.31 (30.90)	−103.44 (−104.48)
10^{-4}	0.04	30	−0.1	36.74 (38.25)	−18.38 (−21.48)
10^{-4}	0.04	30	−0.2	32.14 (34.56)	−7.57 (−9.43)
5×10^{-4}	0.1	80	−0.08	53.98 (59.69)	−104.38 (−115.37)
10^{-4}	0.1	80	−0.08	74.79 (82.10)	−72.79 (−62.69)
2×10^{-5}	0.04	30	−0.018	19.96 (21.06)	−153.68 (−151.03)

TABLE 1. The orientation of ω_F in polar angles for some representative cases, given by θ_F and φ_F. The precession axis is located in the plane $\varphi = 0$. Numbers in brackets are predictions from asymptotic theory. All runs are with $\eta = 0.1$.

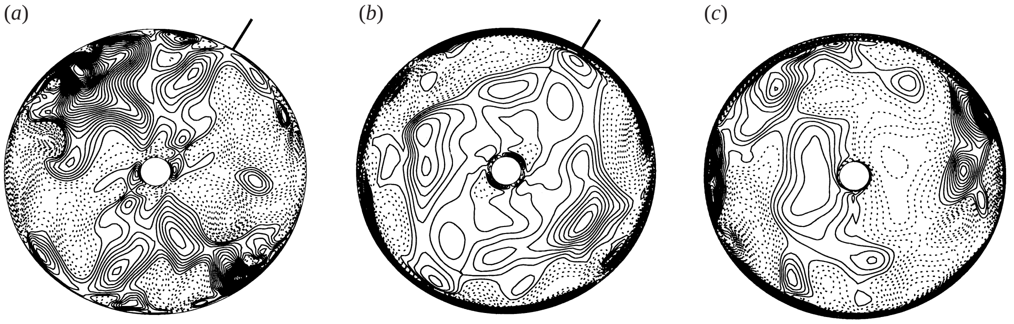

FIGURE 2. (*a*) r-, (*b*) θ- and (*c*) φ-components of $\boldsymbol{u}$ in meridional planes for $\eta = 0.1$, $e = 0.04$, $E = 10^{-4}$, $\alpha = 30°$ and $\Omega = -3 \times 10^{-2}$. More precisely, the (*b*) and (*c*) show u_θ and u_φ in the eastern, but $-u_\theta$ and $-u_\varphi$ in the western hemisphere in order to avoid an artificial change of sign at the z-axis. $\hat{z}$ is pointing up. $\langle \boldsymbol{\omega}_F \rangle$ is directed to the upper right in (*a*) and (*b*) showing u_r and u_θ (as indicated by the straight markers) and is pointing out of the figure in (*c*). Each component is shown in the plane in which it is strongest. The best fitting Poincaré solution has been subtracted. Solid and dashed contour lines indicate positive and negative values respectively.

from critical latitudes well known from linear theory. The critical latitudes are separated by an angle of 60° from the axis of rotation of the fluid. The flow shown in figure 2 is above the threshold of instability and not exactly centrosymmetric for this reason (see the next section).

A most striking feature in experimental visualizations of the laminar flows are cylindrical shear layers coaxial with the rotation axis of the fluid. Figure 3 therefore shows the flow component axisymmetric about $\boldsymbol{\omega}_F$. The shear layers in the zonal velocity well known from experiments clearly appear in the plots. The exact location of the shear layers depends on both the boundary geometry and the Ekman number. The most precise comparison is possible in figure 4 in which the profiles of the zonal velocity in the plane perpendicular to $\boldsymbol{\omega}_F$ are plotted as a function of radius. The strongest shear layer connects the critical latitudes and the positions of the strongest prograde and retrograde jets correspond exactly to those given in figure 3 of Malkus

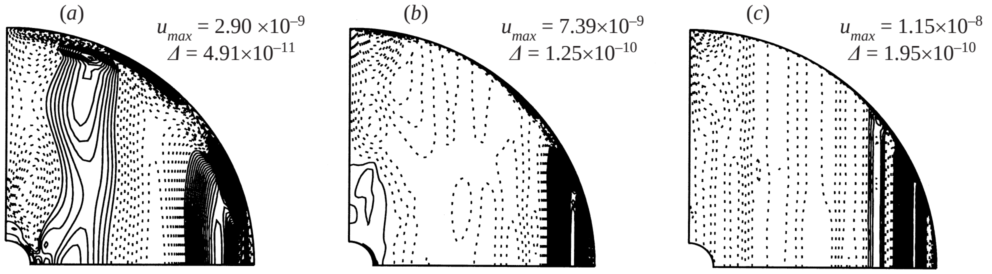

FIGURE 3. Zonal flow component $u_{\varphi'}$ (where φ' denotes the azimuthal angle with respect to the $\boldsymbol{\omega}_F$-axis) axisymmetric about $\boldsymbol{\omega}_F$, after subtraction of the average rotation of the fluid. $\boldsymbol{\omega}_F$ is pointing upwards. $\eta = 0.1$, $e = 0.04$, $\Omega = -10^{-5}$ and $\alpha = 30°$ in all cases. The Ekman number is (*a*) 10^{-4}, (*b*) 10^{-5} and (*c*) 10^{-6}. Contour lines are drawn for levels ranging from $-u_{max}$ to $+u_{max}$. The values of adjacent levels differ by Δ.

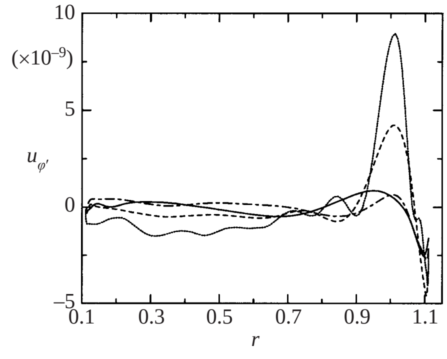

FIGURE 4. $u_{\varphi'}$ from figure 3 in the equatorial plane as a function of r for $\Omega = -10^{-5}$, $\alpha = 30°$ and $\eta = 0.1$. The line styles indicate $e = 0.04$, $E = 10^{-4}$ (solid), $e = 0.04$, $E = 10^{-5}$ (dashed), $e = 0.04$, $E = 10^{-6}$ (dotted), and $e = 0$, $E = 10^{-5}$ (dot dashed). For this last case, $u_{\varphi'}$ has been divided by 100 in order to make the curve fit into the figure.

(1968). The position of the smaller extrema depends on E and a perfect agreement with Malkus' figure cannot be expected for this part of the profile. As can be deduced from figure 4, the prograde jet becomes stronger with decreasing E. According to Busse (1968), a singularity should develop in the limit $E \rightarrow 0$. The Ekman number dependence of the maximum zonal velocity does not follow any simple law valid for the entire interval $10^{-4} < E < 10^{-6}$ but is compatible with a scaling in $E^{-3/10}$ for $10^{-5} < E < 10^{-6}$ (Noir, Jault & Cardin 2001).

With the geophysical application in mind, we briefly revisit the influence of an inner core on the axisymmetric circulation. The issue has already been studied by Tilgner (1999*a*) where plots of the zonal flow axisymmetric about the container axis are shown. In order to complement that investigation, figure 5 shows the zonal flow symmetric about the fluid axis for both spherical and ellipsoidal shells with and without a sizeable inner core. At small precession rates, the angle between the two axes is also small but introduces a few visible differences. The conclusion remains that inclined axisymmetric shear layers appear upon introduction of an inner core. The main cylindrical shear layer is hardly modified by the inner core, but a new one emerges near the critical latitudes of the inner core (figure 5).

The meridional circulation (figure 6) shows that fluid flows from the poles to the equatorial plane along the rotation axis of the fluid. This circulation is symmetric

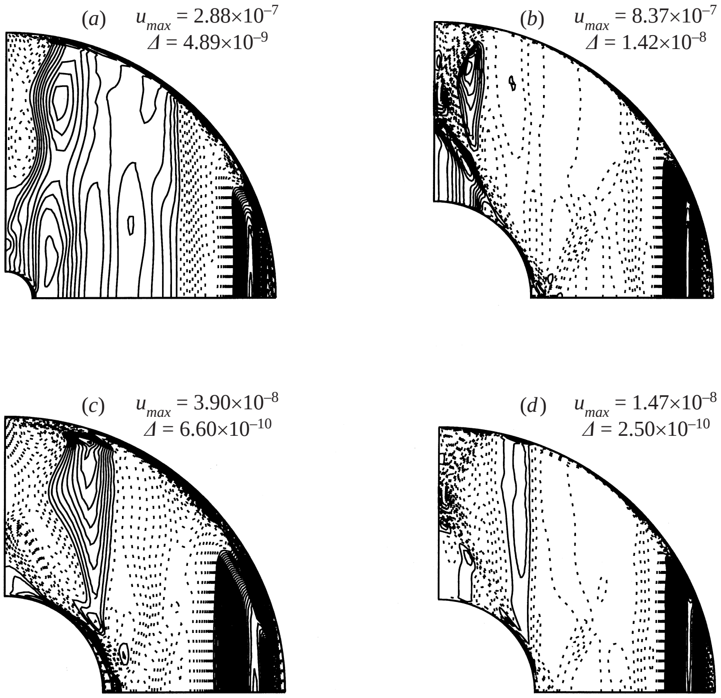

FIGURE 5. $u_{\varphi'}$ as in figure 3 for $\Omega = -10^{-5}$ and $\alpha = 30°$. The remaining parameters are (*a*) $E = 10^{-5}$, $e = 0$, $\eta = 0.1$, (*b*) $E = 10^{-5}$, $e = 0$, $\eta = 0.35$, (*c*) $E = 10^{-4}$, $e = 0$, $\eta = 0.35$, (*d*) $E = 10^{-5}$, $e = 0.04$, $\eta = 0.35$.

with respect to the equatorial plane. Vanyo & Dunn (2000) have observed meridional flow traversing the equatorial plane even in purely laminar flow. This behaviour is not reproduced in our calculations.

Small precession rates have been chosen for figures 1 and 3–6 in order to be sure of obtaining stable flows which can be compared with previous work. Also, for the Earth, $\Omega \approx -10^{-7}$. In this regime, $\omega(r)$ in figure 1 is proportional to Ω and the components in figures 3–6 are proportional to Ω^2. The instability in Malkus' experiments occurs at much higher precession rates. Increasing the precession rate primarily increases the angle between the fluid and container axes. At large enough $|\Omega|$, the velocity field relative to the fluid axis distorts (see figure 2 and compare figures 2 and 4 of Busse & Tilgner (2001) with figure 1). The shape of the zonal velocity profile remains qualitatively the same with a strong prograde jet, but the intensity and exact location of the jet vary with Ω.

4. Instability

The laminar flows of the previous section are all centrosymmetric with respect to the origin, i.e. $\boldsymbol{u}(\boldsymbol{r}) = -\boldsymbol{u}(-\boldsymbol{r})$. The instabilities described in the present section break this symmetry. It is therefore useful to separate the full velocity field into symmetric and antisymmetric components, such that $\boldsymbol{u} = \boldsymbol{u}_a + \boldsymbol{u}_s$ with $\boldsymbol{u}_s = (\boldsymbol{u}(\boldsymbol{r}) - \boldsymbol{u}(-\boldsymbol{r}))/2$ and $\boldsymbol{u}_a = (\boldsymbol{u}(\boldsymbol{r}) + \boldsymbol{u}(-\boldsymbol{r}))/2$. The energy E_a contained in the velocity field $\boldsymbol{u}_a$ is a convenient indicator for the onset of instability. Table 2 lists E_a for runs performed in the unstable regime. Table 3 gives examples of stable flows. Some of the computations use the

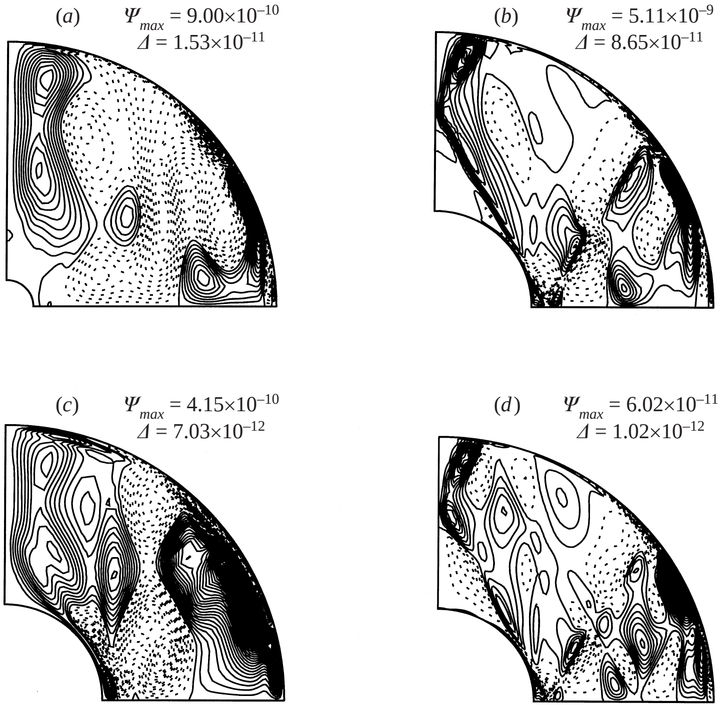

FIGURE 6. Streamlines of the meridional component axisymmetric about $\boldsymbol{\omega}_F$, for the same parameters as in figure 5. Contour lines are drawn for levels ranging from $-\Psi_{max}$ to $+\Psi_{max}$. The values of adjacent levels differ by Δ.

same geometry but higher Ekman numbers than Malkus' experiments. Accordingly, instability sets in at higher precession rates than in the experiments.

Figures 5 and 6 in Vanyo *et al.* (1995) suggest that one should look for disturbances with a well-defined wavenumber with respect to the fluid axis. The velocity fields corresponding to unstable states have therefore been transformed to a coordinate system denoted by primes in which the z'-axis points along $\boldsymbol{\omega}_F$. The field has then been decomposed into spherical harmonics in this new system and the energy contained in the different spectral components has been plotted against the azimuthal wavenumber m'. An example is shown in figure 7. A dominant contribution to $\boldsymbol{u}_a$ occurs at $m' = 7$ and 8, whereas $\boldsymbol{u}_s$ differs little from its shape in stable solutions and certainly does not contain any hint of a wave propagating around the z'-axis. In order to describe the unstable mode and its wavelike character, it is thus enough to consider the structure of $\boldsymbol{u}_a$.

The structure of the instability for the set of parameters used in figure 7 is clarified in figures 8 and 9 and summarized in figure 10. Figures 8 and 9 are snapshots. As time goes on, the $m' = 7$ and $m' = 8$ patterns rotate independently of each other about the z'-axis. Figure 8 shows $u_{az'}$ and u_{ar} in the plane perpendicular to ω_F. $m' = 7$ appears in u_{ar} whereas $m' = 8$ dominates $u_{az'}$. The two sets of rolls overlap but are centred at different radii. Figure 9 shows cylindrical cuts at distances from the fluid axis corresponding to these two radii. For $m' = 7$ one finds columnar vortices symmetric about the equatorial plane of the primed coordinate system, whereas the $m' = 8$ vortices are antisymmetric about this plane.

Figure 10 reproduces these and additional observations in a sketch. Two sets

E	e	α (deg.)	Ω	η	E_{kin}	$\tilde{E}_{kin}$	E_a	Re_{bl}	Ro_{bl}	
5×10^{-4}	0.1	80	−0.08	0.1	0.920	0.115	5.92×10^{-4}	58	0.40	v
5×10^{-4}	0.1	80	−0.2	0.1	1.22	0.20	2.19×10^{-3}	56	0.46	v
10^{-4}	0.1	80	−0.08	0.1	1.33	0.11	1.10×10^{-2}	140	0.46	bl
10^{-4}	0.04	30	−0.03	0.1	0.373	2.25×10^{-2}	4.25×10^{-4}	91	0.25	v,bl
10^{-4}	0.04	30	−0.035	0.1	0.49	3.1×10^{-2}	8.1×10^{-4}	104	0.28	v,bl
10^{-4}	0.04	30	−0.05	0.1	0.573	3.70×10^{-2}	1.56×10^{-3}	113	0.31	v,bl
10^{-4}	0.04	30	−0.1	0.1	0.512	3.18×10^{-2}	6.25×10^{-4}	107	0.31	v,bl
10^{-4}	0.04	30	−0.2	0.1	0.435	3.27×10^{-2}	9.38×10^{-4}	94	0.30	v,bl
2×10^{-5}	0.04	30	−0.018	0.1	0.161	4.44×10^{-3}	5.00×10^{-6}	109	0.16	v,bl
7×10^{-4}	0	60	−0.2	0.01	0.609	0.12	7.67×10^{-5}	54	0.34	v
5×10^{-4}	0	60	−0.1	0.01	0.509	6.79×10^{-2}	5.21×10^{-4}	45	0.32	v
10^{-4}	0	40	−0.05	0.1	0.500	3.14×10^{-2}	4.25×10^{-4}	104	0.28	v,bl

TABLE 2. Parameters for the simulations in ellipsoids and a few runs in spherical geometry near the onset of instability. E_{kin} is the total energy in the mantle frame, $\tilde{E}_{kin}$ the energy in components other than W_1^0 and W_1^1 (equations (15), (20)), and E_a the energy of $\boldsymbol{u}_a$. Re_{bl} and Ro_{bl} are the Reynolds and Rossby numbers of the boundary layer. The last column states whether the instability occurred in the boundary layer (bl) or in the volume (v). Resolutions ranged from 65 to 129 Chebychev polynomials and from 64 to 128 for the highest order of retained spherical harmonics. The highest included azimuthal wavenumbers ranged from 32 to 64.

E	e	α (deg.)	Ω	η	E_{kin}	$\tilde{E}_{kin}$
5×10^{-4}	0.1	80	−0.03	0.1	7.63×10^{-2}	7.94×10^{-3}
10^{-4}	0.1	80	−0.01	0.1	1.03×10^{-2}	5.42×10^{-4}
10^{-4}	0.04	30	−0.01	0.1	1.84×10^{-2}	1.01×10^{-3}
3×10^{-5}	0.04	30	−0.01	0.1	2.65×10^{-2}	8.90×10^{-4}
2×10^{-5}	0.04	30	−0.01	0.1	2.85×10^{-2}	7.98×10^{-4}
10^{-5}	0.04	30	−0.001	0.1	1.96×10^{-4}	3.68×10^{-6}
5×10^{-4}	0	60	−0.07	0.01	3.94×10^{-1}	4.78×10^{-2}
10^{-4}	0	30	−0.01	0.1	5.48×10^{-2}	3.31×10^{-3}

TABLE 3. Same as table 2 but for runs below the onset of instability.

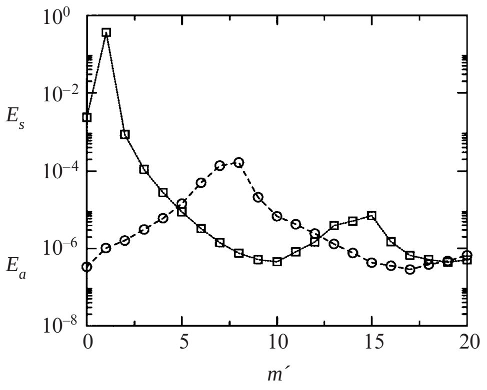

FIGURE 7. Energy contained in the modes with wavenumber m' as a function of m' for $\eta = 0.1$, $e = 0.04$, $\alpha = 30°$, $\Omega = -0.03$ and $E = 10^{-4}$. Antisymmetric (circles) and symmetric (squares) contributions are shown separately.

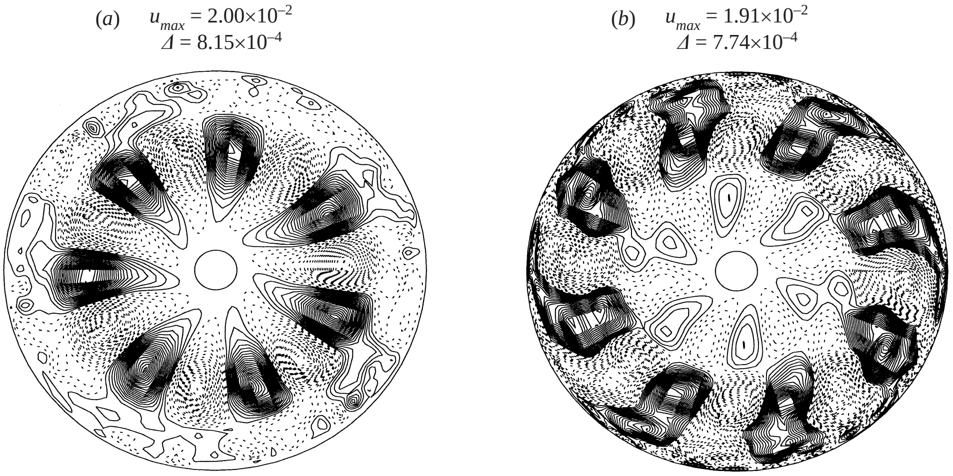

FIGURE 8. (*a*) u_{ar} and (*b*) $u_{az'}$ in the plane perpendicular to $\boldsymbol{\omega}_F$ for the same parameters as in figure 7. Contour level separation and values of the extreme levels are given.

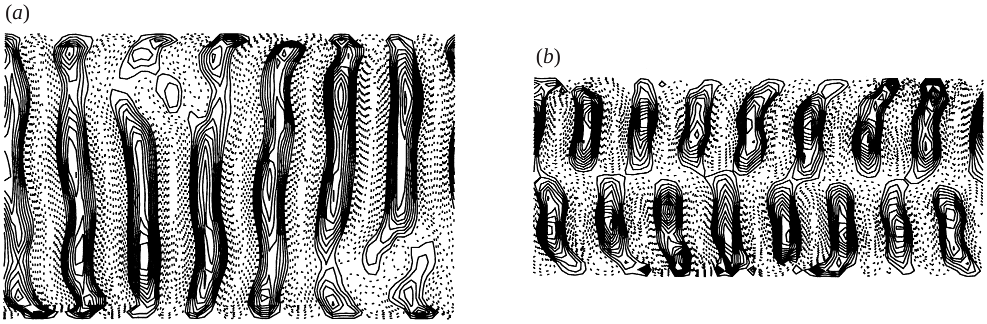

FIGURE 9. u_{ar} on cylindrical surfaces at distances 0.638 (*a*) and 0.869 (*b*) from the $\boldsymbol{\omega}_F$-axis for the same case as in figures 7 and 8. φ' runs from $-\pi$ to π in going from left to right and the lattitude varies vertically from $-55°$ to $+55°$ (*a*) and from $-40°$ to $+40°$ (b).

of columnar vortices centred at different distances from the fluid axis exist, with wavenumbers differing by one. The entire pattern is antisymmetric with respect to reflection at the origin. Individual rolls in the wave with odd wavenumber therefore have equal vorticity in the northern and southern hemispheres. Rolls belonging to the wave with even wavenumber on the contrary have opposite vorticities in both hemispheres. The designations north and south refer of course to the primed coordinate system. The axial and azimuthal components in the outer roll pattern are of comparable magnitude, whereas $u_{az'}$ is small in the component with odd m'. $u_{az'}$ reaches its extremal values in between the outer vortices.

The same sketch is valid for other parameters, except that the values of m' change as indicated in table 4. In one case, three adjacent values of m' are listed. Visual inspection of the corresponding flow reveals only two sets of rolls, because the superposition of the waves with the highest and lowest m' (these two modes have the same symmetry with respect to the equatorial plane) merely appears as a time-dependent distortion of the wave with the highest m'. It has been verified that all three modes drift independently of each other.

E	e	α (deg.)	Ω	η	m'	$\omega_{m'}$	T	$\lvert\boldsymbol{\omega}_F\rvert$
10^{-4}	0.04	30	−0.03	0.1	7,8	$\omega_7 = 6.28$, $\omega_8 = 6.23$	0.50	0.888
5×10^{-4}	0.1	80	−0.08	0.1	3,4	$\omega_3 = 1.90$, $\omega_4 = 1.76$	1.71	0.614
5×10^{-4}	0	60	−0.1	0.01	2,3,4	$\omega_2 = 2.15$, $\omega_3 = 2.12$, $\omega_4 = 2.12$	1.48	0.681

TABLE 4. Details of the modes excited near the onset of instability. m' and $\omega_{m'}$ are the wavenumber and drift frequency of these modes with respect to the rotation axis of the fluid. In a frame in which the precession and container axes are fixed and the fluid axis points along z', the temporal and azimuthal dependence of the waves is given by $\exp(\mathrm{i}(m'\varphi' - \omega_{m'}t))$. In this frame, the fluid rotates at angular velocity $|\boldsymbol{\omega}_F|$. The $\omega_{m'}$ have been determined from equatorial sections such as in figure 8 plotted for different moments in time. The energy of the flow oscillates with the period T.

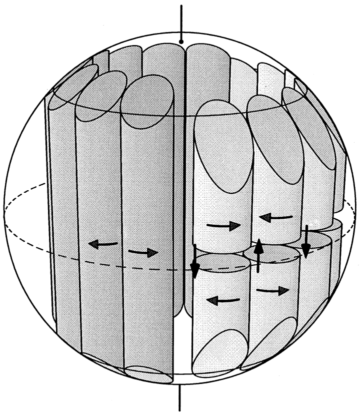

FIGURE 10. Sketch of the structure of the unstable mode in figures 8 and 9.

In the precessing primed coordinate system of figures 7–10, in which the fluid axis is along z' and the precession axis $\hat{\boldsymbol{\Omega}}$ and container axis $\hat{z}$ are stationary, the separate equations of motion for $\boldsymbol{u}_a$ and $\boldsymbol{u}_s$ become

$$\frac{\partial}{\partial t}\nabla \times \boldsymbol{u}_s + \nabla \times [(\nabla \times \boldsymbol{u}_s) \times \boldsymbol{u}_s + (\nabla \times \boldsymbol{u}_a) \times \boldsymbol{u}_a] + 2\nabla \times (\boldsymbol{\Omega} \times \boldsymbol{u}_s) = E\nabla^2\nabla \times \boldsymbol{u}_s, \quad (21)$$

$$\frac{\partial}{\partial t}\nabla \times \boldsymbol{u}_a + \nabla \times [(\nabla \times \boldsymbol{u}_s) \times \boldsymbol{u}_a + (\nabla \times \boldsymbol{u}_a) \times \boldsymbol{u}_s] + 2\nabla \times (\boldsymbol{\Omega} \times \boldsymbol{u}_a) = E\nabla^2\nabla \times \boldsymbol{u}_a. \quad (22)$$

If $\boldsymbol{r}$ is a vector to a point on the boundary, $\boldsymbol{u}_s = \hat{z} \times \boldsymbol{r}$ and $\boldsymbol{u}_a = 0$ on the boundary. The boundary conditions thus drive only $\boldsymbol{u}_s$. If $\boldsymbol{u}_a$ is strictly zero initially, it will stay zero forever: $\boldsymbol{u}_a$ can only grow as an instability of a ground state $\boldsymbol{u}_s$. Once a pair of modes has been excited in $\boldsymbol{u}_a$, it drives through the $(\nabla \times \boldsymbol{u}_a) \times \boldsymbol{u}_a$ term in (21) a symmetric motion at the double wavenumber. The corresponding spectral peak is seen in figure 7. The onset of instability is also manifested as small-amplitude oscillations of the energy. Even for the runs in table 4, the oscillation is not exactly harmonic but an underlying period T can be discerned which is given in that table. The sum of the two angular frequencies of a pair of modes is nearly $2\pi/T$.

It is tempting to classify the vortices which are symmetric with respect to the equatorial plane as Rossby waves. There are three candidates in table 4 (with $\omega_{m'}$ equal to 6.28, 1.90 and 2.12). From the drift frequencies in that table, the frequency ω_R in the frame of the fluid is computed as $\omega_R = \omega_{m'} - m'|\boldsymbol{\omega}_F|$. For the three sets

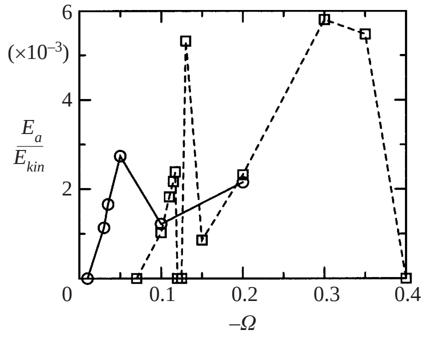

FIGURE 11. The ratio of the antisymmetric energy E_a and the total kinetic energy E_{kin} as a function of the precession rate Ω for $E = 10^{-4}$, $e = 0.04$, $\eta = 0.1$, $\alpha = 30^\circ$ (circles) and $E = 5 \times 10^{-4}$, $e = 0$, $\eta = 0.01$, $\alpha = 60^\circ$ (squares).

of symmetric vortices, one therefore finds values for ω_R of 0.064, 0.058 and 0.077, respectively. These numbers are within 0.05 of the frequency computed for a Rossby wave localized at the distance from the axis at which the observed disturbance is maximum (equation (4.55) of Gubbins & Roberts 1987). A better agreement cannot be expected because of the uncertainties in the determination of $\omega_{m'}$ and because the observed motion is not localized well at a certain cylindrical radius as is assumed in the theoretical formula. Note also that these three values of ω_R are all positive as must be the case for Rossby waves. The same calculation for the antisymmetric vortices yields mostly negative ω_R.

Figure 11 shows two series of simulations in which $|\boldsymbol{\Omega}|$ has been systematically increased. Surprisingly, the energy can drop back to zero for $|\boldsymbol{\Omega}|$ above the instability threshold. One could suspect that an instability shows in the symmetric components at these parameters, but this is not the case. There is on the other hand no obvious reason why the instability should occur only in $\boldsymbol{u}_a$. Indeed, for $E = 10^{-4}$, $e = 0.04$, $\alpha = 30^\circ$ and $\Omega = -0.035$, the instability resides in modes with $m' = 6$ and 7, the symmetric components containing more energy than the antisymmetric ones.

Away from the onset, an increasingly complex time dependence of the flow is observed and the main peak in spectra like shown in figure 7 becomes broader. Increasing $|\boldsymbol{\Omega}|$ or E generally shifts the energy content to lower m'. The cases presented by Tilgner & Busse (2001) are similar to the one in table 2 with $E = 7 \times 10^{-4}$ and have most energy in modes with $m' = 0$ and 1.

Independently of the dynamics of the bulk fluid, the Ekman layers may become unstable. This is demonstrated in figure 12 which shows as a function of radius the density $\epsilon_a(r)$ of the energy contained in $\boldsymbol{u}_a$ averaged over spherical surfaces:

$$\epsilon_a(r) = \frac{1}{4\pi} \int_0^{\pi} \mathrm{d}\theta \sin\theta \int_0^{2\pi} \mathrm{d}\varphi \tfrac{1}{2} \boldsymbol{u}_a^2. \tag{23}$$

Three different situations are represented in figure 12. Either only the bulk has become unstable in the manner described above, or only the boundary, or both. One instability does not seem to affect the other. The parameters for which the boundary layer instability has been observed are listed in table 2. It is natural to look at the Reynolds number of the boundary layer in order to determine a criterion for the onset of this instability. The distance from the boundary at which the absolute value of the radial velocity (averaged over the corresponding spheroidal surface) reaches a maximum is used as the boundary layer thickness. The layer thickness

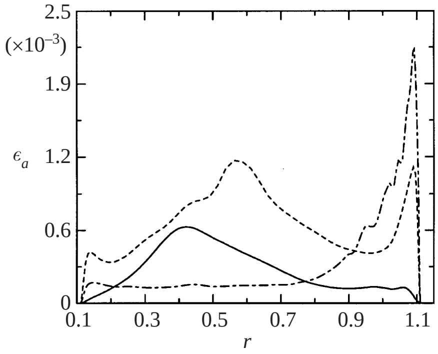

FIGURE 12. The energy density ϵ_a of the antisymmetric components (equation (23)) as a function of r for $E = 5 \times 10^{-4}$, $e = 0.1$, $\alpha = 80°$, $\Omega = -0.08$ (solid), $E = 10^{-4}$, $e = 0.04$, $\alpha = 30°$, $\Omega = -0.05$ (dashed), and $E = 10^{-4}$, $e = 0.1$, $\alpha = 80°$, $\Omega = -0.08$ (dot dashed). The values for the last curve have been divided by ten. $\eta = 0.1$ for all cases.

is approximately $1.4 \times E^{1/2}$ in all cases. Based on this thickness and the maximum tangential velocity, the Reynolds numbers listed in table 2 have been computed. The Rossby numbers have been estimated as $v_h[2(1 + \Omega \cos \alpha)]^{-1}$ where v_h is the maximum tangential velocity at the edge of the boundary layer. The critical Reynolds number lies somewhere in between 50 and 100, which falls into the range quoted by Tatro & Mollo-Christensen (1967) for time-independent Ekman layers. Figure 13 gives an impression of the unstable boundary layer flow. The comparatively small lateral length scales of the motions excited by the boundary layer instability become difficult to resolve at more extreme parameters. The development of this instability and ensuing numerical instabilities turn out to be the most serious obstacle to high precession rates at low E.

The classification of the bulk instability is more arduous. It is known from theoretical work (Pierrehumbert 1986; Gledzer & Ponomarev 1992) that an inertial instability occurs in flows with elliptically deformed streamlines, and through related mechanisms in precession-driven flow in ellipsoidal cavities (Kerswell 1993). This work is not directly relevant here because the same type of instability is observed in simulations in both spherical and ellipsoidal geometries. Incidentally, the criterion for the onset of instability given by Kerswell (1993) predicts stability for all the simulated flows.

A variation of these analyses allows one to see that the bulk instability is due to flow components with wavenumber $m' = 1$. Following the presentations given by Gledzer & Ponomarev (1992) and Kerswell (1993), consider the inertial mode problem posed by (21) and (22) appropriately linearized if $\boldsymbol{u}_s$ is a solid body rotation plus a perturbation of wavenumber $m' = 1$. Two eigenmodes of the unperturbed problem with time and azimuthal dependences given by $\exp(\mathrm{i}(m'_a\varphi' - \omega_a t))$ and $\exp(\mathrm{i}(m'_b\varphi' - \omega_b t))$ are coupled by the perturbation only if $|m'_a - m'_b| = 1$. Since the basic state has no time dependence in the chosen frame of reference, the strongest coupling occurs if the resonance condition $\omega_a = \omega_b$ is met. The instability thus consists of at least one pair of inertial modes with wavenumbers differing by one and nearly equal frequencies. Looking at table 4, one sees that these conditions are fulfilled, with two pairs of resonant modes being excited in one case. It seems highly unlikely that such a constellation of modes would be excited accidentally by an $m' = 0$ disturbance of the basic flow which could have instabilities consisting of a single inertial mode of arbitrary wavenumber and frequency.

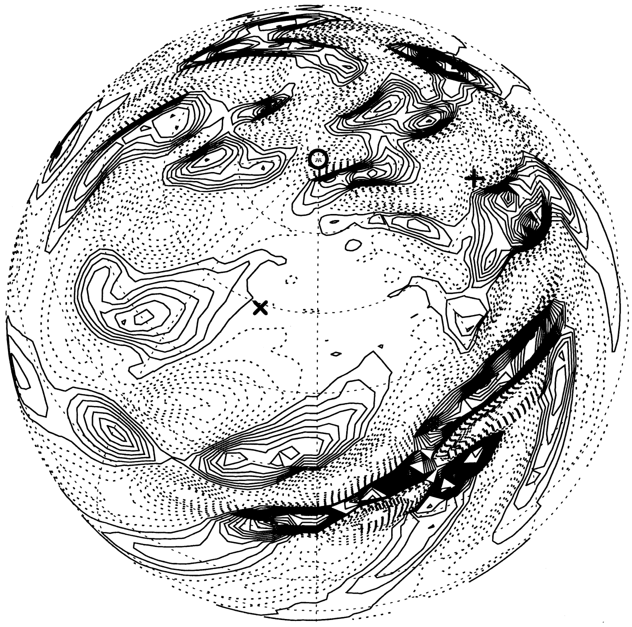

FIGURE 13. u_{ar} on a surface separated by 0.015 from the outer boundary for $e = 0.04$, $\eta = 0.1$, $E = 10^{-4}$ and $\Omega = -0.03$. The north pole is marked by a circle, the fluid axis by an $\times$ and the precession axis by a $+$. Contour levels are separated by 3.56×10^{-4} and range from -1.05×10^{-2} to 1.05×10^{-2}.

Experimental reports, on the contrary, suggest that the axisymmetric internal cylindrical shear layers cause an instability even though the employed visualization methods cannot ascertain whether these shear layers merely act as tracers or whether they actually trigger an instability. In all the simulations discussed so far, the $m' = 1$ deviations from a flow with uniform vorticity in the basic state outweight the $m' = 0$ deviations. However, as the Ekman number is decreased, the viscous corrections contributing to the $m' = 1$ deviations diminish, whereas the axisymmetric shear layer connecting the critical latitudes becomes more and more singular. An instability of that shear layer is thus plausible at low E. One can determine the typical velocity difference in the $m' = 1$ component from plots such as in figure 1 and construct a Rossby number from it. It turns out that this Rossby number increases with decreasing Ekman number, so that the mechanism related to the $m' = 1$ components should remain effective even at the lower Ekman numbers at which the axisymmetric shear layer possibly becomes unstable too.

According to the picture delineated by the simulations described in this section, at least two essentially independent instability mechanisms coexist. The strongest departures from a solution with constant vorticity are in the toroidal components of wavenumber 0 and 1 with respect to the fluid axis as presented in § 3 and in Tilgner & Busse (2001). If the bulk flow becomes unstable it could presumably do so because of both components but only instabilities triggered by the wavenumber 1 deviations have actually been observed. This instability breaks the inversion symmetry of the flow and leads to a time dependence of the total energy. Since the excited flow fills a large fraction of the fluid volume, the origin of the instability cannot be traced back to a more particular feature of the velocity field, such as for example the critical latitudes. In addition, the boundary layer becomes unstable independently if its Reynolds number is large enough (certainly if it is larger than 100). The unstable modes vary seemingly continuously in going from ellipsoidal to spherical containers so that the container shape does not matter. In the sphere, the Poincaré solution is a solid body rotation which is a stable flow, so that viscous corrections to the Poincaré flow must be responsible for the instabilities. It is expected on theoretical grounds (Kerswell 1993) that in ellipsoidal containers, inertial instability also occurs due to the shape of the boundaries. There is no evidence for this mechanism (nor should there have been according to theory) in the parameter range accessible with the method used here. This last scenario has been linked to Malkus' second experiment in which a sudden transition with an abrupt increase of the driving torque as well as hysteresis occurred. None of these effects have been seen in the simulations. On the contrary, the motions excited by the instability always accounted for only a small fraction of the total energy (see table 2).

5. Conclusion

We have reported on direct simulations of precession-driven flow in spheroidal shells. The range of parameters accessible with the employed numerical method is limited mainly by the onset of a boundary layer instability accompanied by unresolvably small scales. The bulk becomes unstable independently through the excitation of motions reminiscent of Rossby waves as summarized in figure 10. The energy contained in the unstable mode always remained small compared with the total energy and has not been large enough for dynamo action. In the attempts at simulating a precession-driven dynamo made so far, the initial magnetic field was converted by interaction with the flow into a strong toroidal field which eventually decayed.

Experiments coupled with theory have already suggested that the wavy instability exists in the Earth (Malkus 1971). In the experiments, the boundary layer is very thin and its instability has not been seen. Such an instability should exist in the Earth, however. The data on the orientation of the average vorticity of the flow show that one can apply with confidence the formula of Busse (1968) to the Earth. According to this theory, the angle between the Earth's axis of figure and the rotation axis of the core is 10^{-5} which leads to velocities at the core–mantle boundary of up to $2.5\,\mathrm{mm\,s^{-1}}$. This is one order of magnitude larger than the velocities deduced from the secular variation of the magnetic field. The precessional velocity field varies with the period of one day and the mantle of course screens variations of the magnetic field on that time scale. Nonetheless, these large velocities have an influence on the boundary layer dynamics. Based on a critical Reynolds number for the boundary layer of 100 and using $1.4 \times E^{1/2}$ for the layer thickness, the Earth's Ekman layer must be unstable if the Ekman number of the Earth's core is less than 2×10^{-14}, which is the case according to current estimates.

This work was supported by the Deutsche Forschungsgemeinschaft. Most of the simulations presented here have been run on the CRAY T3E parallel machines of the John von Neumann Institute for Computing and the High Performance Computing Center Stuttgart.

REFERENCES

Busse, F. 1968 Steady fluid flow in a precessing spheroidal shell. *J. Fluid Mech.* **33**, 739–751.

Gledzer, E. & Ponomarev, V. 1992 Instability of bounded flows with elliptical streamlines. *J. Fluid Mech.* **240**, 1–30.

Gubbins, D. & Roberts, P. H. 1987 Magnetohydrodynamics of the Earth's Core. In *Geomagnetism Vol. 2* (ed. J. A. Jacobs), pp. 1–183. Academic Press.

Kerswell, R. 1993 The instability of precessing flow. *Geophys. Astrophys. Fluid Dyn.* **72**, 107–144.

Malkus, V. 1968 Precession of the earth as the cause of geomagnetism. *Science* **160**, 259–264.

Malkus, V. 1971 Do precessional torques cause geomagnetism? In *Mathematical Problems in the Geophysical Sciences*. Lectures in Applied Mathematics, Vol. 14, pp. 207–228. Springer.

Noir, J., Jault, D. & Cardin, P. 2001 Numerical study of the motions within a precessing sphere, at low Ekman number. *J. Fluid Mech.* **437**, 283–299.

Pierrehumbert, R. 1986 Universal short-wave instability of two-dimensional eddies in an inviscid fluid. *Phys. Rev. Lett.* **57**, 2157–2159.

Poincaré, H. 1910 Sur la précession des corps déformables. *Bull. Astronom.* **27**, 321–356.

Tatro, P. & Mollo-Christensen, E. 1967 Experiments on Ekman layer instability. *J. Fluid Mech.* **28**, 531–543.

Tilgner, A. 1999*a* Magnetohydrodynamic flow in precessing spherical shells. *J. Fluid Mech.* **379**, 303–318.

Tilgner, A. 1999*b* Non-axisymmetric shear layers in precessing fluid ellipsoidal shells. *Geophys. J. Intl* **136**, 629–636.

Tilgner, A. 1999*c* Spectral methods for the simulation of incompressible flows in spherical shells. *Intl J. Numer. Meth. Fluids* **30**, 713–724.

Tilgner, A. & Busse, F. 2001 Fluid flows in precessing spherical shells. *J. Fluid Mech.* **426**, 387–396.

Vanyo, J. & Dunn, J. 2000 Core precession: flow structures and energy. *Geophys. J. Intl* **142**, 409–425.

Vanyo, J., Wilde, P., Cardin, P. & Olson, P. 1995 Experiments on precessing flows in the earth's liquid core. *Geophys. J. Intl* **121**, 136–142.